

Evaluating pixel-based vs. object-based image analysis approaches for lithological discrimination using VNIR data of WorldView-3

Samira SHAYEGANPOUR¹, Majid H. TANGESTANI (✉)¹, Saeid HOMAYOUNI², Robert K. VINCENT³

¹ Department of Earth Sciences, Faculty of Sciences, Shiraz University, Shiraz 7196484334, Iran

² Centre Eau Terre Environnement, Institut National de la Recherche Scientifique, Québec QCJ3X1S2, Canada

³ Department of Geography, Bowling Green State University, Ohio 43403-0001, USA

© Higher Education Press 2021

Abstract The object-based against pixel-based image analysis approaches were assessed for lithological mapping in a geologically complex terrain using Visible Near Infrared (VNIR) bands of WorldView-3 (WV-3) satellite imagery. The study area is Hormuz Island, southern Iran, a salt dome composed of dominant sedimentary and igneous rocks. When performing the object-based image analysis (OBIA) approach, the textural and spectral characteristics of lithological features were analyzed by the use of support vector machine (SVM) algorithm. However, in the pixel-based image analysis (PBIA), the spectra of lithological end-members, extracted from imagery, were used through the spectral angle mapper (SAM) method. Several test samples were used in a confusion matrix to assess the accuracy of classification methods quantitatively. Results showed that OBIA was capable of lithological mapping with an overall accuracy of 86.54% which was 19.33% greater than the accuracy of PBIA. OBIA also reduced the salt-and-pepper artifact pixels and produced a more realistic map with sharper lithological borders. This research showed limitations of pixel-based method due to relying merely on the spectral characteristics of rock types when applied to high-spatial-resolution VNIR bands of WorldView-3 imagery. It is concluded that the application of an object-based image analysis approach obtains a more accurate lithological classification when compared to a pixel-based image analysis algorithm.

Keywords object-based image analysis, pixel-based image analysis, lithological mapping, Worldview-3, Hormuz Island, spectral angle mapper, support vector machine

1 Introduction

Producing the lithological maps has undergone continuous evolution associated with technological improvements in relative fields. At the current time, advances in sensor technology and developments in image processing approaches are the two main improvements in collecting geological data and lithological mapping. Many researchers have recently used multispectral data such as thematic mapper (TM) (Mather et al., 1998), operational land imager (OLI), and advanced spaceborne thermal emission and reflection radiometer (ASTER) to extract information about rocks and alterations as well as their spatial distribution (e.g., Naghadehi et al., 2014; Ducart et al., 2016; Ibrahim et al., 2018; Noori et al., 2019; Bolouki et al., 2019). Although the pixel size of 30 m in Landsat and ASTER SWIR imagery is not appropriate for producing a large-scale and accurate geological map, they are beneficial for reconnaissance mapping to guide geologists for more detailed field observations and mappings (Sun et al., 2017; Testa et al., 2018; Bedini, 2019; Rajendran and Nasir, 2019). However, the WorldView-3 (WV-3) satellite has recently provided alternative operational data that could efficiently be applied for large-scale mapping of terrestrial features, including lithological units.

This satelliteborne sensor benefits from significant improvements such as high spatial resolution (1.24 m in VNIR and 3.7 m in SWIR bands), more spectral bands (16 multispectral bands), and high geometric and radiometric accuracies associated with high radiometric resolution (11-bit in VNIR and 14-bit in SWIR bands) than the ASTER data. As a result, WV-3 data have been recently utilized by remote sensing geologists in various disciplines. Mars (2018) applied band ratios and Logical Operator

Algorithms (LOAs) on data of WV-3 to map goethite, calcite and dolomite, epidote-chlorite, and muscovite, using the absorption features of Fe^{3+} , CO_3^{2-} , Fe-Mg-OH, and Al-OH, respectively, in Mountain Pass, California. Ye et al. (2017) assessed the capabilities of WorldView-3 data compared to the ASTER and OLI imagery for lithological mapping using a support vector machine (SVM) algorithm. They estimated higher accuracies of 17% and 14% for WV-3 data outputs than, respectively, ASTER and OLI data, and attributed it to higher spatial resolution of WV-3 bands. Sun et al. (2017) enhanced the alteration minerals in the Pobei area of Xinjiang Uygur Autonomous Region, China, using short wave infrared data of WorldView-3. These authors proposed five principal component analysis (PCA) models and ten mineral indices for enhancing the alteration minerals. The WorldView-3 and ASTER TIR data were applied by Bedini (2019) for mineral mapping in the Rodalquilar deposits, Spain. It was expressed that the geographic dispersal of goethite was successfully enhanced by combining all VNIR bands and band-1 of the SWIR region of WV-3 and suggested that ASTER TIR data could map quartz-rich zones.

The primary remote sensing contexts such as training data and statistical assumptions are used to classify images by running algorithms such as supervised vs. unsupervised, parametric vs. non-parametric, per-pixel vs. sub-pixel, and pixel-based image analysis (PBI) vs. object-based image analysis (OBIA) (Thapa and Murayama, 2009). To date, most geologists have used pixel-based methods to map rock units, in which, they classified lithology based on per pixel or sub-pixel formats without considering the contextual data for neighboring pixels (e.g., Hewson et al., 2017; Ayoobi and Tangestani, 2018; Liu et al., 2018). In per-pixel classification algorithms, each image pixel is independently assigned to a unique lithology if the spectrum of pixel and the desired lithological end-member is highly suited. (Elnagheeb and Bromley, 1994). Two well-known algorithms being used for per-pixel mapping of geological targets are spectral angle mapper (SAM) (Kruse et al., 1993) and spectral feature fitting (SFF) (Clark and Roush, 1984). However, they lead to ignoring the spatial correlations between pixels of the imagery. Moreover, spatial information can supply extra information related to the shape and size of different structures, which could help identify and classify surface features with high accuracy. Blaschke (2010) has concluded that the object-based image analysis (OBIA) approach delineates a remarkable classification method for remote sensing objectives. In OBIA, several attributes or features are associated with each of the image objects, and these attribute values can be derived from the imagery. The selection of an optimal set of features for the classification of unknown image objects is a crucial step and is very important for designing a useful classification system (Cai et al., 2018).

Recently, the OBIA approach has extensively been

applied to enhance and map the Earth's surface features. For instance, Petropoulos et al. (2012) investigated the capability of OBIA and SAM methods for land use/land cover mapping in a heterogeneous Mediterranean land using Hyperion imagery. They estimated a higher overall accuracy and Kappa coefficient for OBIA results. Additionally, the forest waste due to the gold excavation in Guyana was evaluated by Mengisteab et al. (2014) using OBIA on the Landsat data, during which, they effectively enhanced and specified the minor mining activities at the area.

Moreover, few articles have already been published on the geological utilizations of OBIA. Van der Werff et al. (2007) applied Observatoire pour la Mineralogie, l'Eau, la Glace et l'Activite (OMEGA) data for geological mapping on Mars using an object-based processing method. Grebby et al. (2016) illustrated that object-based image analysis method could successfully map the rock types in an area covered by vegetation. They applied the Airborne LiDAR (Li) and Airborne Thematic Mapper-9 (ATM9) data and discriminated chalky marl, pillow lava, dyke, and alluvium-colluvium deposits. Aufaristama et al. (2017) mapped the Krafla volcanic rocks of the Icelandic volcanic zone by the use of OBIA and spectral angle mapper (SAM) methods on Landsat 8 and SPOT-5 images. They revealed that SAM was successful in producing detailed lava surface morphology maps; however, it partly led to a salt-and-pepper effect. They concluded that despite the more efficient results of OBIA approach, it is sensitive to the objects derived from image segmentation. The mapping of geological structures such as lineaments and faults was analyzed by OBIA method in south-west England (Yeomans et al., 2019) using the high resolution airborne geophysics and LiDAR data. They suggested that OBIA method is highly effective for lineament detection.

An overview of the published articles indicated that geologists have conventionally used PBI methods for enhancement and identification of rock types, methods that are generally performed based on the spectral characteristics of desired features. Unlikely, in the object-based image analysis approach, the segmentation of image data into homogeneous and consistent segments is a prerequisite for classification (Hay and Castilla, 2008; Lang et al., 2008; Blaschke, 2010). The spatial dimensions, including parameters such as distances, neighborhoods, and topologies, are important in the OBIA approach, which is a primary reason for increase in its usage in recent years (Benz et al., 2004; Blaschke et al., 2004).

Despite the advantages reported for the OBIA approach (Castillejo-González et al., 2009; Petitjean et al., 2012; Matton et al., 2015), rare publications are available on its performance on the WV-3 data for discriminating lithological features. This paper investigated the potential of the object-based approach (support vector machine) and compared it to a pixel-based approach (spectral angle mapper) for classification and information extraction of

lithological units in Hormuz Island, southern Iran. This island is a geologically salt dome, and is well-known for its particular setting and varying types of exposed rocks and minerals. Considering that the VNIR bands of WorldView-3 can detect the dominant spectral features of rock outcrops of the study area, this data set was applied for this research. The classification accuracies were subsequently analyzed and compared by parameters of confusion matrices and the Kappa coefficients.

2 Geological setting

The study area, Hormuz Island, is an Iranian island in the Persian Gulf with an oval shape and a total area of about 45 km² (Fig. 1). A concentric structure shown at the central part of the island contains salt, gypsum, and anhydrite (Elyasi et al., 1975), surrounded by salt rocks. The salt

rocks contain abundant fragments of black shale, black and white dolomite, limestone to sandy limestone, iron oxide-rich strata, as well as outcrops of igneous rocks dominantly consisting of tuff, rhyolite, and trachyte (Faramarzi et al., 2015). Stocklin (1972 and 1974) suggested that the diapirism of Hormuz salt plugs has moved the vast enclaves of igneous rocks to the surface; now occurring as isolated outcrops.

An iron oxide-rich band surrounded by young sediments wraps around the island. Alluvial deposits that have been demolished from upstream formations are dominantly outspread in the northern half of the Island (Fig. 1), and expand as small patches in other parts. The Hormuz ochre is the most significant mine on the island, with a reservoir of about 390000 tons (Yazdi et al., 2014). In terms of quality and applications in industry, this red-colored earth pigment is considered a unique raw material (Aqanabati, 2006).

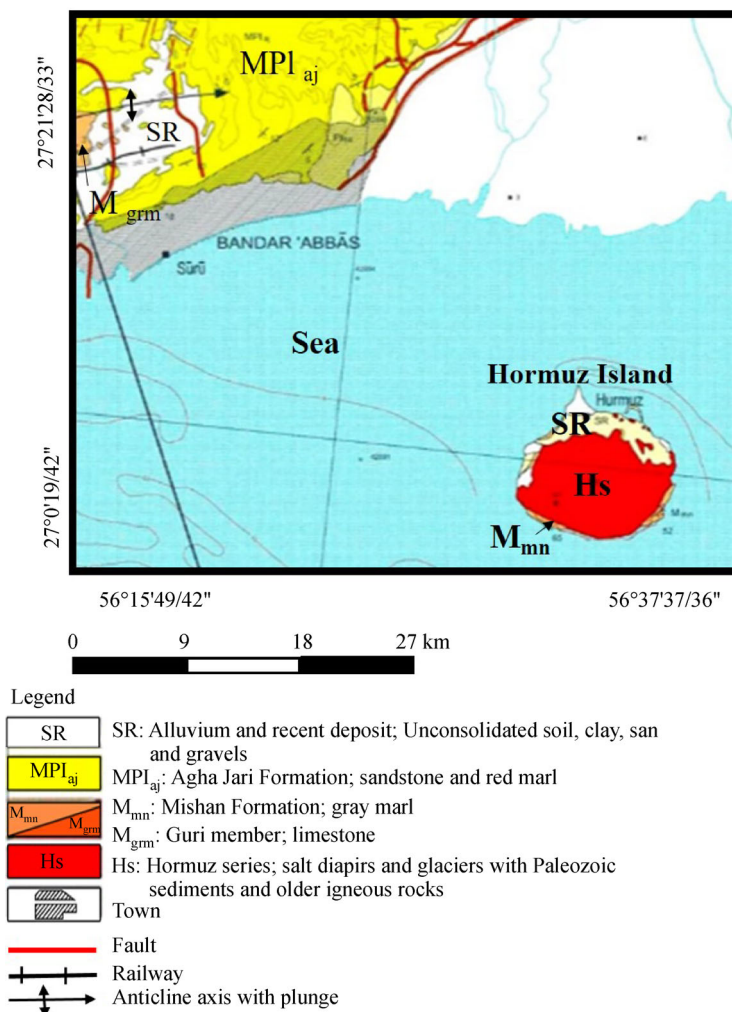


Fig. 1 The study area in 1:250000 geological map (Fakhari, 1994).

3 Materials and methods

3.1 Overview

The recently launched WorldView-3, is a high spatial and spectral resolution satellite that operates at a height of near 617 km. This satellite provides one panchromatic and eight multispectral bands in the VNIR region, eight bands in SWIR region, and 12 CAVIS (Clouds, Aerosols, Vapors, Ice, and Snow) bands with pixel sizes of, respectively, 0.31 m, 1.24 m, 3.7 m, and 30 m (Kuester, 2016).

The VNIR data of WorldView-3, utilized in this study, were acquired on June 16, 2016 (available at Worldview3 website). These data were first corrected for likely geometric and atmospheric errors, and subsequently, were applied in PBIA and OBIA approaches by the use of SAM and SVM algorithms for classifying the lithology of Hormuz Island.

The WV-3 level 2-A data have already been calibrated and corrected for radiometric and geometric inaccuracies. The datum WGS-84 was used to geo-referencing applied data to UTM zone 40-north projection. The data were also atmospherically corrected using FLAASH model, available in ENVI software, version 5.3. The effects of seawater and tidal zone on the images were eliminated by applying a masking method. Data processing was supported by extensive field sampling combined with petrographic and spectroscopic studies to identify mineralogy and lithology of rock types. Finally, the accuracy of results was assessed by the use of field criteria and confusion matrices.

3.2 Field sampling and laboratory studies

According to the field observations, spectroscopy, petrography, and X-ray Diffraction (XRD) studies, the rock units were classified into five groups, including: 1) mixture of red soil, gypsum, and anhydrite, 2) mixture of red soil, tuff and anhydrite, 3) white rhyolite tuff, 4) diabase and volcanic tuff, and 5) marl. The validation sites of these lithological features were identified, and 5–10 spectra in the range of 400 nm to 2500 nm were measured for each sample collected from study area, using an ASD FieldSpec spectrometer, available in the spectral laboratory of the Department of Geography, Bowling Green State University, the USA, which were subsequently averaged for each lithology. The pictures of hand samples and their averaged spectra, resampled to the VNIR bands of WV-3, are shown in Figs. 2 and 3. Hormuz Island is dominantly formed of red soil and salt rock (Figs. 2(a), 2(b), and 2(h)). The red color of soil is due to the extensive occurrence of hematite, which decreases in amount and the extent from center to the margins of the island. The major absorption features of red soil and gypsum in their high-resolution spectra are in 1900 nm attributed to the H₂O vibration in anhydrite and gypsum, and 800 nm, because of the charge-transfer effect

of ferric iron (Hunt, 1980) (Figs. 3(a) and 3(b)). The second most dominant rock unit is red soil with large amounts of tuff and less anhydrite (Figs. 2(b), 2(e), and 2(h)). The tuffaceous rocks include rhyolite tuff, alkaline rhyolite tuff, and dacite tuff (Figs. 3(a) and 3(b)). Microscopic studies showed that tuffaceous rocks consist mainly of quartz, alkaline feldspar, muscovite, chlorite, and rare epidote and goethite, which are the results of degradation of ferromagnesian minerals (Mahyari, 2016).

The measured spectra of white rhyolite tuff displayed an absorption in 800 nm for charge transfer effect of Fe³⁺ (Hunt, 1980) and additional features in 2160 nm and 2330 nm attributed to vibrational modes of Al-OH and Mg-OH (Salisbury and Hunt, 1974) (Figs. 3(a) and 3(b)). Moreover, the diagnostic absorption features of diabase in 400–500 nm and 650–800 nm could be attributed to charge transfer effect of Fe-O (Hunt, 1980). Similar spectral properties of this rock type in 2200 nm and 2210 nm are due to Mg-OH vibrational processes (Segal, 1983) (Fig. 3(a)). The carbonate interlayers are observed in marl outcrops of the Mishan Formation (Fig. 2(g)) and also are dispersed western and south western the island within a sequence of salt and gypsum. The typical absorption feature of marl is near 2300 nm (Hunt, 1980); however, high-resolution spectra of its samples showed significant absorptions in 2000 nm and 2200 nm (Fig. 3(a)) due to Al-OH vibrations (Huang and Kerr, 1960) as well as an insignificant absorption feature near 1900 nm, for H₂O (Hunt, 1980) (Figs. 3(a) and 3(b)).

3.3 Pixel-based image analysis (PBIA)

PBIA is a spectrum space method that classifies the imagery by finding the analogy of a reference spectrum to that of a target (Richards, 1993). Spectral characteristics of desired materials play an essential role in their detection, identification, and classification. The appropriate spectra are typically selected from spectral libraries or field samples and are imported to an algorithm. Figure 4 shows a general workflow of the PBIA approach; its practical procedure is described in subsections “end-member selection” and “classification.” In cases where no information is available for a class, the spectral measures could be examined on a single signature vector basis to determine the spectral similarity between the target and the reference. This commonly is applied for discrimination and identification of specific features, but not for classifying an imagery (Kruse et al., 1993). Moreover, these references are efficient only if, compared with the spectral features, are true characteristics of desired materials.

3.3.1 End-member selection

A reference spectrum or end-member, which represents the known spectral class, should typically be selected and put

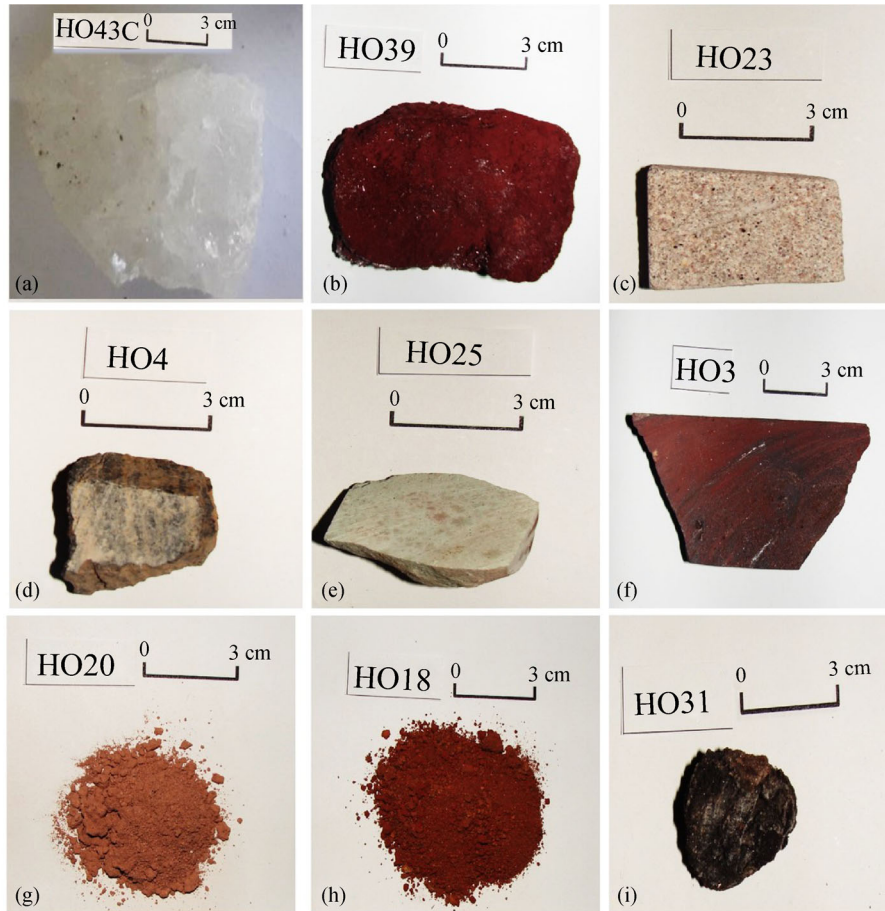


Fig. 2 Hand samples of: (a) salt rock, (b) iron oxide, (c) rhyolite, (d) diabase, (e) green tuff, (f) basalt, (g) marl, (h) iron soil, and (i) volcanic tuff.

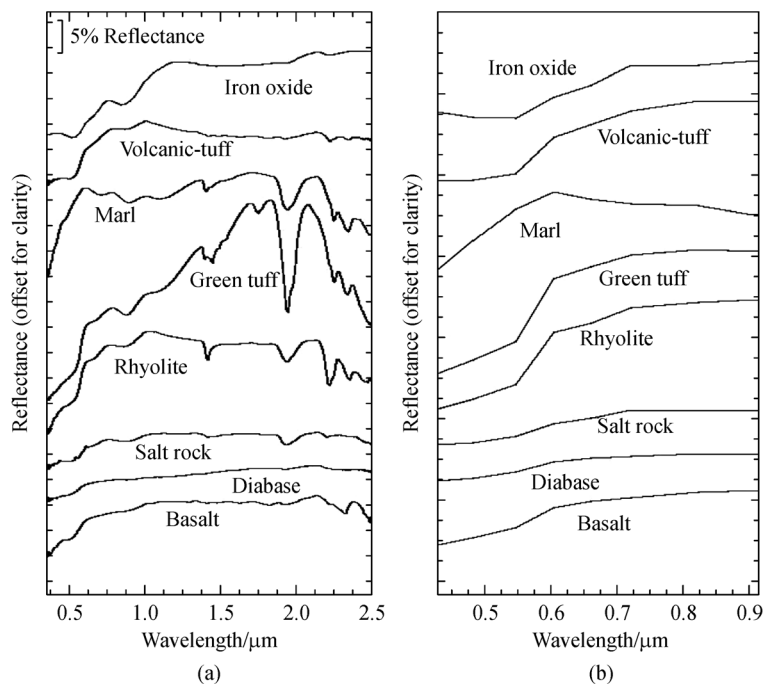


Fig. 3 (a) High-resolution spectra of rock samples, (b) spectra of rocks resampled to the VNIR bands of WV-3.

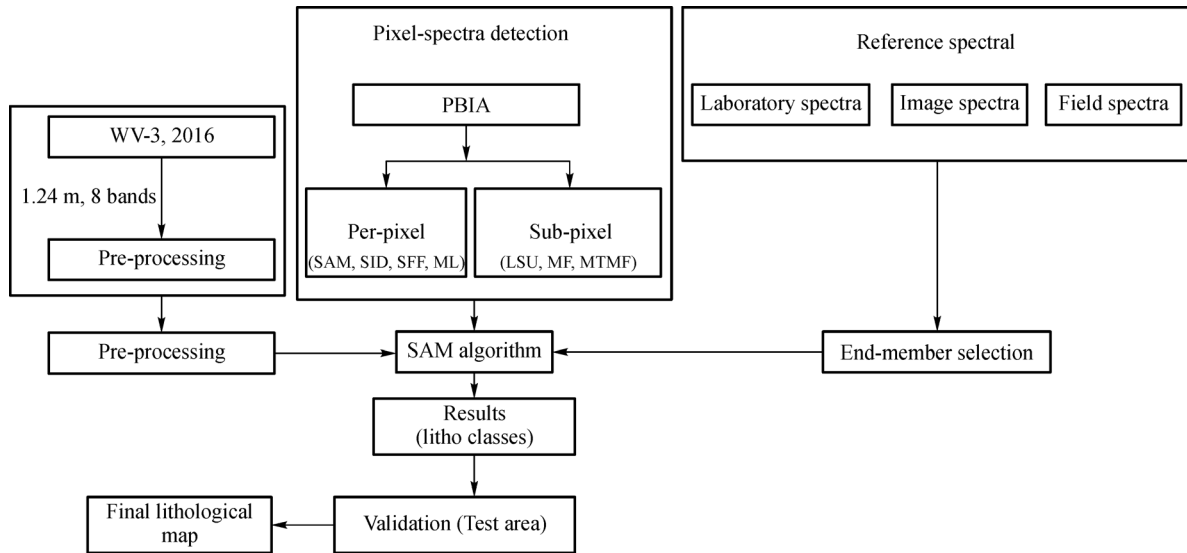


Fig. 4 Flowchart of the PBIa approach (PBIa = pixel-based image analysis; WV-3 = WorldView-3; SAM = spectral angle mapper; SID = spectral information divergence; MF = matched filtering; MTMF = mixture tuned matched filtering, ML = maximum likelihood, SFF = spectral feature fitting, LSU = linear spectral un-mixing)

into the SAM algorithm when analyzing the desired satellite data. The end-members are generally selected from spectral libraries or are extracted from applied imagery. Since the image spectra involve the atmospheric conditions of the applied data set, it is suggested that reference spectra from imagery are usually more valid for detecting the targets than those selected from libraries (Wang et al., 2004). On the other hand, the spectra extracted from imagery do not show subtle spectral features, as is evident in reference spectra of spectral libraries (Wang et al., 2004). In this study, six reference spectra of lithological features were directly extracted from WV-3 imagery (Fig. 5) using the Z-profile tool available in ENVI software. The representative sites of desired pixels were identified during field observations (Fig. 6) and appropriate rock samples were collected for further investigations.

3.3.2 Spectral angle mapper (SAM) algorithm

This algorithm is categorized as a pixel-based image analysis technique and has extensively been applied by the remote sensing geologists (e.g., Qiu et al., 2006; Rajendran et al., 2013; Markoski and Rolim, 2014). Kruse et al. (1993) indicated that this algorithm could identify the similarity between a pixel of a data set and the reference spectra by calculating a spectral angle (“ α ” in Eq. (1)) between them. They suggested two n-dimensional spectral vectors for this algorithm (Eq. (1)), coincided with the spectrum of each pixel (r) and the spectrum of desired end-member (t); in which the number of dimensions are equal to the number of applied bands.

$$\alpha = \cos^{-1} \left(\frac{\sum_{i=1}^n t_i r_i}{(\sum_{i=1}^n t_i^2)^{1/2} (\sum_{i=1}^n r_i^2)^{1/2}} \right). \quad (1)$$

The pixels with lower spectral angles represent closer similarity to the reference spectrum and appear darker (Research Systems, Inc., 2002; Jensen, 2005). For the propose of lithological mapping, eight bands of WV-3 and the spectra of six previously identified lithological groups were put into the SAM algorithm. Subsequently, the different threshold values per end-member spectrum were examined, and finally, the appropriate pixels attributed to particular lithology, were realized based on the lowest spectral angles for the desired end-member.

3.4 Object-based image analysis (OBIA)

The objects in scale of satellite imagery are various sets of similar pixels that provide the necessary information for the object-based image analysis method. These are similar groups of pixels based on their spectral characteristics such as texture, shape, or color, and conditions of surrounding pixels (Tormos et al., 2012). The general workflow for this approach, presented in Fig. 7, includes: 1) segmenting the image, 2) sample selection by the use of a stratified random scheme (Mason et al. 1988), 3) feature selection for scale using correlation-based feature selection (CFS) method (Dorren et al., 2003), 4) classifying the image using SVM classifier (Hsu et al., 2007).

This algorithm defines the decision borders by giving priority to margins between support vectors that spatially contain a minor geometric error (Borges, 1998; Melgani and Bruzzone, 2004). An important issue for performing

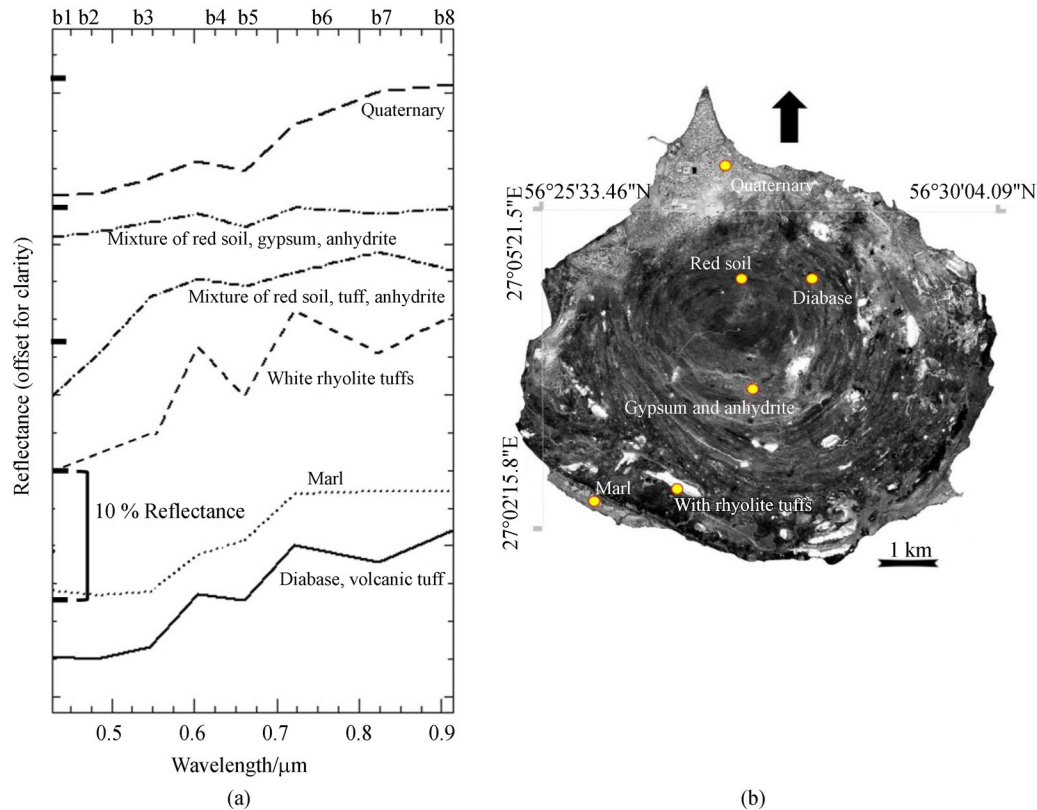


Fig. 5 (a) Spectral curves of lithological groups, extracted from VNIR bands of WV-3, and (b) locations and the names of collected end-members in a gray image.

this algorithm is selection of suitable kernel function, which works with two other parameters including Gamma and “C”. Hsu et al. (2007) indicated that the kernel function re-projects the varying space and C-factor controls the degree of misclassification by SVM. They expressed that this algorithm randomly fixes the complex decision borders with particular spatial specifications using the C-factor. On the other hand, Hsu et al. (2007) specified that the Gamma factor adapts the spread kernel function and that the factor that both determines the spread of the kernel function and controls the susceptibility of the decision boundary to confused support vectors, is set by C parameter. Geologists such as Bahrambeygi and Moeinzadeh (2017) and Gasmi et al. (2016) have already used the object-based images analysis approach in lithological mapping.

3.4.1 Segmentation

The primary step before performing the object-based image analysis for lithological classification is image segmentation, which leads to generating non-overlapping polygons. The critical factor for defining the lithological segments is a scale that determines the accuracy of image segmentation. Marceau (1999) suggested that exert of different scales in imagery could be possible if the

dimensions of desired object is larger than the pixel size. To create the appropriate lithological segments in applied imagery, several scales were tested from scale parameters of 5 to 20 considering the pixel size of 1.24 m for WV-3 data and the sizes of objects. Finally, a scale parameter of 10 was selected to be applied to segmenting the image at one scale for any lithological class. If the value of scale parameter is high, it obtains larger objects.

Blaschke et al. (2004) indicated that imagery could be categorized into comparatively analogous and important classes of pixels by an appropriate segmentation algorithm. These segments are subject to be identified using a competent processing technique and converted into relevant objects. Parameters of color and shape control the homogeneity criteria, in which the summation of factor values is equal to 1 for each couple.

The degree of analogy in texture is determined by shape, which is a combination of smoothness and compactness, and helps extract the desired objects (Trimble, 2015). Considering that in lithological segmentation, we would instead, give the most crucial role to spectral information, the ratio 0.9/0.1 was set to color/shape. Moreover, the ratio 0.5/0.5 was set for smoothness/compactness because we were reluctant to support the smooth or rough segments, and the value 1 was assigned as the weight of the image layer to prevent any prejudice.



Fig. 6 Field photos of (a) red soil and marl, (b) anhydrite and marl, (c) tuff, (d) anhydrite and rhyolite, (e) red soil, gypsum and anhydrite, (f) diabase, (g) gypsum, (h) marl.

3.4.2 Training/Test sampling

A significant phase after segmentation of the image and before implementing object-based image analysis algorithm is selecting the various rock units that are going to play the role of training samples. Sampling schemes such as systematic, cluster, simple random, and stratified random have already been used by various algorithms (Congalton and Green, 2009). In this study, the selection of lithological training samples was based on the stratified random sampling with the purpose of selection of enough number of polygons for each distinguished lithology group. When performing this sampling method at the scale parameter of 10, the visual and field interpretations of

lithological features were used as references for obtaining deduced knowledge of areas. The main issue in stratified random sampling strategy is the correct lithological interpretation of the area for which we used the previous studies (e.g., Mahyari, 2016), and field observations. The geological map and GPS points of field observations were then overlapped on the segmented layer to assign a class label to each segmented object.

3.4.3 Features and feature selection

The object-based method produces more features than pixel-based approach due to its logic in engaging the segmented objects. The frequently used features by

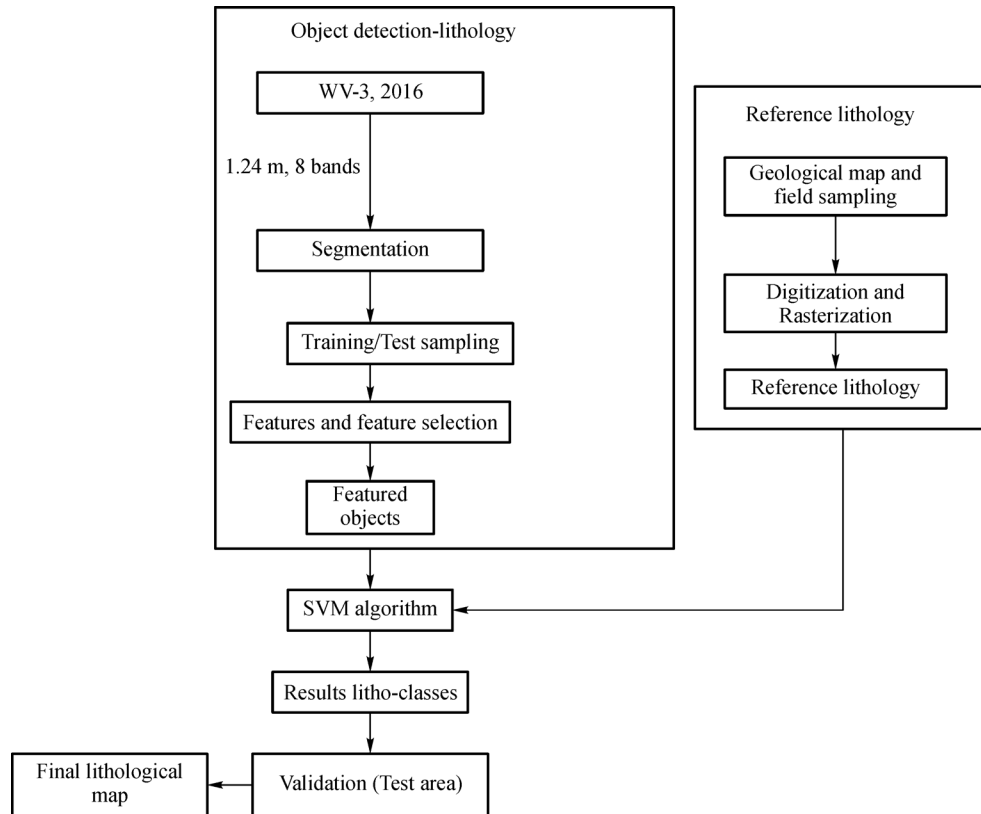


Fig. 7 Flowchart of the OBIA approach.

eCognition software, version 9.0 (Trimble, 2015) including spectral measure, shape, and texture, were directly calculated using WV-3 bands. The spectral measures including mean, max, mode, difference, standard deviation, and brightness were calculated for each lithology using aerosol, blue, green, yellow, red, red edge, NIR1, and NIR2 bands. The shape measures consisting of area, roundness, main direction, density, compactness, rectangular fit, elliptic fit, border index, shape index, and asymmetry were also calculated. Furthermore, the texture measures including Gray-Level Co-occurrence Matrix (GLCM), homogeneity, and Gray-Level Difference Vector (GLDV) were estimated on the basis of pixels of every lithology. On the basis of WV-3 bands, other texture parameters consisting of contrast, dissimilarity, entropy, standard deviation, correlation, mean, GLDV angular second moment, entropy, mean, and contrast were also measured.

3.4.4 Support vector machine (SVM)

The classification method applied in this study (support vector machine) works based on the hypothesis of machine learning through a supervised learning process. This algorithm isolates two desired classes and enlarges the space between them by creating a hyperplane (Kavzoglu and Colkesen, 2009). This method is based on the belief of

maximum margin (Fig. 8), which is the distance between identified boundary for classes and the closest samples, and the idea of transforming extent of depiction on the applied data set into an extent of excessive size. The support vectors are intended samples positioned adjacent to the borders of decision (Fig. 8) (Oommen et al., 2008). Four types of kernels including linear, sigmoid, polynomial, and radial basis function (RBF), execute the concept of transformation of the SVM algorithm (Hsu et al., 2007).

The SVM algorithm defines the decision borders by giving priority to margins between support vectors that

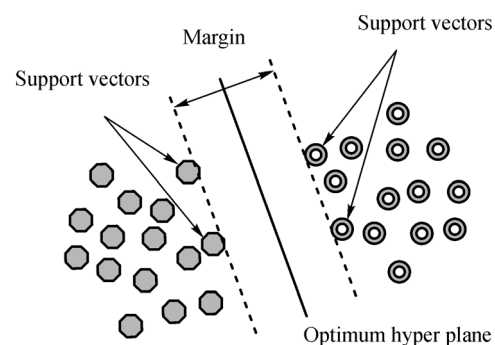


Fig. 8 The optimum hyperplane, margin, and support vectors in the SVM algorithm (Kavzoglu and Colkesen, 2009).

contain a minor geometric error in space (Borges, 1998; Melgani and Bruzzone, 2004). An essential issue for performing this algorithm is the selection of suitable kernel function, which works with two other parameters including gamma and “C”. Karatzoglou et al. (2004) stated that when performing SVM algorithm, the varying space is re-projected by kernel function, and C-factor directs the level of misclassification. They described that this algorithm randomly fixes the complex decision borders having particular structural specifications by using the C-factor; in which these structures are a basis of support vector positions in varying space. Karatzoglou et al. (2004) also expressed that the extent of the kernel task is balanced by the Gamma factor, and C parameter sets the item that determines the extent of the kernel task; this parameter also modifies the susceptibility and the decision boundary to those support vectors which are confused.

Although many types of kernels are available for the SVM, the RBF was applied in this study because it is suggested as a suitable primary option (Karatzoglou et al., 2004).

3.5 Assessing the accuracy of results

The degree of correspondence between PBIA and OBIA classification results and the field and laboratory evidences were assessed for evaluate the lithological plausibility of each classifier output. A random sampling of rock types provided a set of samples that were then spectrally and petrographically analyzed to verify their lithology. The overall accuracy of results was estimated based on a confusion matrix (Congalton and Green, 2009). In this regard, the reference sites with 5023 pixels for SAM and 5949 pixels for SVM algorithms were selected through

visual interpretation of the images associated with the general in situ and laboratory validations.

4 Results and discussion

4.1 PBIA results

To enhance the desired lithological units by spectral angle mapper, various threshold values were examined for spectral angles and the maximum angle of 0.1 in the range of 0.0–1.0 was set acceptable. To produce a lithological map (Fig. 9) from SAM output images, a classification code was assigned to each pixel based on its closest match to the reference spectrum (Kruse et al., 1993; Boardman and Kruse, 1994). The output image shows spatial overlaps for rhyolite and marl units (green and brown pixels). The marl units are more extended eastern and northern the study area in the output image, than what was observed in the field. The mixtures of red soil, tuff, and anhydrite are not well discriminated thought the area. The Quaternary deposits that are mostly extended at the northern parts of the island, are misclassified as a salt and pepper mixture. Furthermore, a great circular area peripheral to the central yellow class (Fig. 9) is not attributed to any lithological unit (gray pixels). The overall accuracy parameter of a confusion matrix was used to assess the validity of lithological map achieved by this classifier.

4.2 OBIA results

To discriminate the lithological units, six lithological codes were assigned to extracted objects in SVM classifier. The

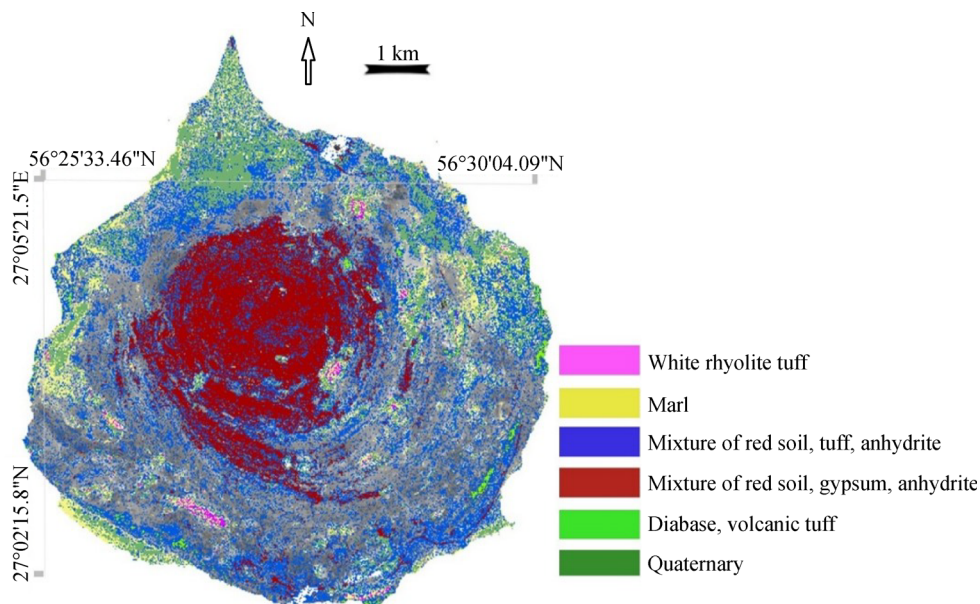


Fig. 9 Classification map of lithological units in Hormuz Island using the spectral angle mapper algorithm.

gamma and C parameters were set to 0 and 2, and the final classification map was produced by the use of original WV-3 data set (Fig. 10). In general, this output map showed the lithological extensions and borders more clear and transparent than SAM output, and the whole area was successfully divided into assigned lithological classes. The highest similarity in shape and extent of the classes in output images of the two methods (Figs. 9 and 10) belongs to the mixed class “red soil, gypsum and anhydrite” with a circular shape at the central part of the Hormuz Island. However, the shape, size, borders, and structures of other lithological units are significantly different in two output maps considering that they are highly explicit and recognizable in map produced by SVM (Fig. 10). This method was capable of achieving reliable results by considering the specific spectral absorption and reflection features of desired objects and their textures and spatial relationships. The various lithological types and the Quaternary sediments were also successfully discriminated via the segmentation process performed based on appropriate training areas, even in few numbers. Furthermore, field observations and controls showed that the lithological units extracted by SVM method are more precise than the results obtained by SAM technique. Results obtained by SVM demonstrated that lithology classification based on the texture features and spectral characteristics of a high spatial resolution data such as WV-3 outstandingly outperforms the pixel-based image analysis approaches such as SAM technique. The accuracy of lithological classes obtained by this classifier were assessed and presented in the next section using the overall accuracy of a confusion matrix.

4.3 Accuracy assessment

Table 1a shows the confusion matrix of results obtained by the SAM, compared to the ground truths obtained via field observations. It showed that the SAM has accurately mapped the diabase with volcanic tuff class that occur in central and eastern parts of the study area, with a user’s accuracy of 82.35% and producer’s accuracy of 78.87% (Table 1a). A mixture of red soil, gypsum, and anhydrite was classified with producer’s accuracy of 70.20% and the user’s accuracy of 58.82%. However, the moderate user’s accuracies of mixture of red soil, gypsum, and anhydrite, white rhyolite tuff, and Quaternary deposits could be attributed to the similarity in spectral characteristics of this lithological classes in applied bands of WV-3. Table 1b reveals the confusion matrix of the SVM output. Results showed that the object-based mapping method has been magnificently more accurate in mapping the white rhyolite tuff and mixtures of red soil, tuff and anhydrite with user’s accuracies of 84.14% and 92.13% and producer’s accuracies of 89.16% and 75.02%. The overall accuracies for SAM and SVM results were 70.16 and 86.03, respectively (Table 1).

4.4 Discussion

The primary purpose of this study was to compare the performance of a pixel-based image analysis approach versus an object-based approach in lithological mapping of a complex terrain. The capability of approaches in discriminating lithological units was evaluated by the use of a confusion matrix parameters (Table 1). Results

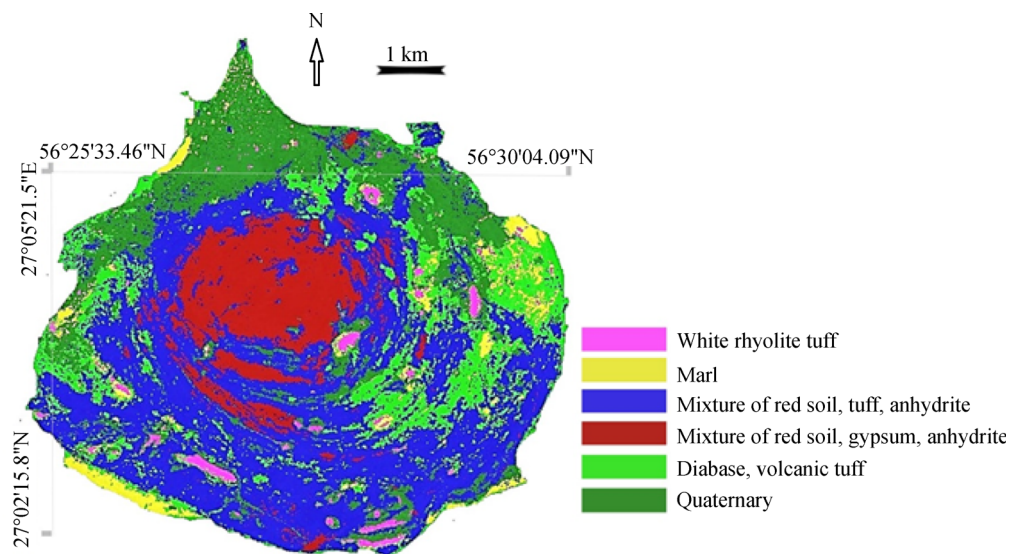


Fig. 10 Classification map of lithological units in Hormuz Island as produced by the SVM algorithm.

Table 1 Confusion matrices for SAM (a) and SVM (b) classification methods.

a)	SAM	MRGA	MRTA	DVT	WRT	M	QD	Total (Pixels)	User.ac.
MRGA		490	153	0	110	0	80	833	58.82
MRTA		88	510	0	60	180	130	968	52.68
DVT		120	0	560	0	0	0	680	82.35
WRT		0	0	150	530	110	130	920	57.60
M		0	0	0	188	650	119	957	67.92
QD		0	0	0	0	220	475	695	68.34
Total (Pixels)		698	663	710	888	1160	934	5023	64.61
Prod.ac.		70.20	76.92	78.87	59.68	56.03	50.85	65.42	75.71

Notes: Overall accuracy = 70.16%. (MRGA: Mixing of red soil, gypsum and anhydrite; MRTA: Mixing of red soil, tuff and anhydrite; DVT: Diabase with volcanic tuff; WRT: white rhyolite tuffs; M: MARL; and QD: Quaternary deposits)

b)	SVM	MRGA	MRTA	DVT	WRT	M	QD	Total (Pixels)	User.ac.
MRGA		870	130	0	0	0	0	1000	87.00
MRTA		70	820	0	0	0	0	890	92.13
DVT		0	50	1150	90	0	0	1290	89.14
WRT		0	0	59	741	78	0	878	84.39
M		0	93	0	0	667	71	831	80.26
QD		0	0	0	0	180	880	1060	83.01
Total (Pixels)		940	1093	1209	831	925	950	5949	85.98
Prod.ac.		92.55	75.02	95.11	89.16	72.10	92.63		86.09

Notes: Overall accuracy = 86.03%. (MRGA: Mixing of red soil, gypsum and anhydrite; MRTA: Mixing of red soil, tuff and anhydrite; DVT: Diabase with volcanic tuff; WRT: white rhyolite tuffs; M: MARL; and QD: Quaternary deposits)

showed that the object-based approach outperformed the pixel-based method with an average difference of 19.33% in overall accuracy.

The spectral-based techniques involve two drawbacks: 1) extraction of spectra from known pure materials, 2) calibration of the pixel spectrum. These techniques are performed based on an approach in which the pixel spectrum is compared to the spectra of a known pure material. Spectra of these materials are generally extracted from imagery or measured of field-collected samples, and if needed, they are selected from known spectral libraries. Methods for extraction of spectra from imagery typically search for pure pixels. Although these methods depend on the size of pixels, such pixels might be rare on the surface. Therefore, the numerical values of these spectral end-members may commonly be associated with noise. This noise shows that spectral discrimination is devalued when a pixel is a mixture of two rock types occurring next to each other.

With recent advances in capabilities of the satellite data such as in WV-3, more studies are focusing on the texture of images and extraction of contextual information that is a measure of association between the values of neighboring pixels (Marceau et al., 1990; Hay and Niemann, 1994). In comparison to the pixel-based methods that only rely on the DN values of pixels, segments in object-based

approaches obtain extra information on the spatial behavior of the objects, which makes it more advantageous (Blaschke and Strobl, 2001; Darwish et al., 2003). Consequently, it is suggested that the object-based methods are more efficient than per-pixel algorithms for mapping the various rock units because the decrease of intra-class variability happens when averaging the DN values of all nearby pixels within objects such as rock classes.

Depending on the type of classifier and the input data set, the efficiency of object-based image analysis methods for target enhancement such as in the case of a lithology, could be different; although, in general, this approach outperforms the pixel-based methods. Another fact for such variability is that a unique value of scale is not perfect for segregating all the lithological categories.

The improved enhancement and discrimination of Quaternary deposits, marl, rhyolite, a mixture of red soil, tuff and anhydrite, and a mixture of red soil, gypsum and anhydrite in this study (Figs. 9 and 10), revealed that the object-based image analysis method is superior over that of the pixel-based approach. In the OBIA classification map, correct spatial distribution is displayed for rhyolite, marl, Quaternary deposits, a mixture of red soil, tuff and anhydrite, and a mixture of red soil, gypsum, and anhydrite. The detection of Quaternary deposits has not

always been as easy as other units. This is mainly because it is a combination of various products of weathering and erosion of upstream outcrops. The visual interpretation of output results in Fig. 11(a) confirms the improvements of OBIA method in enhancement and discrimination of lithological units and attributing all pixels to desired classes. Moreover, Fig. 11(b) displays that considering the importance of intra-class discrepancies for OBIA and similarity in the spectral properties in the PBIA method, the white rhyolite class is efficiently classified by OBIA; however, it is misclassified by PBIA with marl unit. This drawback is also observed for other classes in outputs of the SAM algorithm. Meanwhile, the map produced by

SAM gives necessarily lower pixel numbers per class than SVM. Also, a geological unit outcropping in small areas, would also give a low number of pixels per class, both for SAM and SVM.

Besides, Fig. 11(c) shows that the object-based method was successful in decreasing the salt-and-pepper pixels associated with spectral-based mapping. The common issues in low-resolution pixels are the heterogeneity in spectral properties of rock units and spectral differences between rocks, vegetation, and Quaternary deposits, in cases that all are present in one pixel.

When generating the attributes of objects such as rock types, in the OBIA approach, the spectral characteristics of

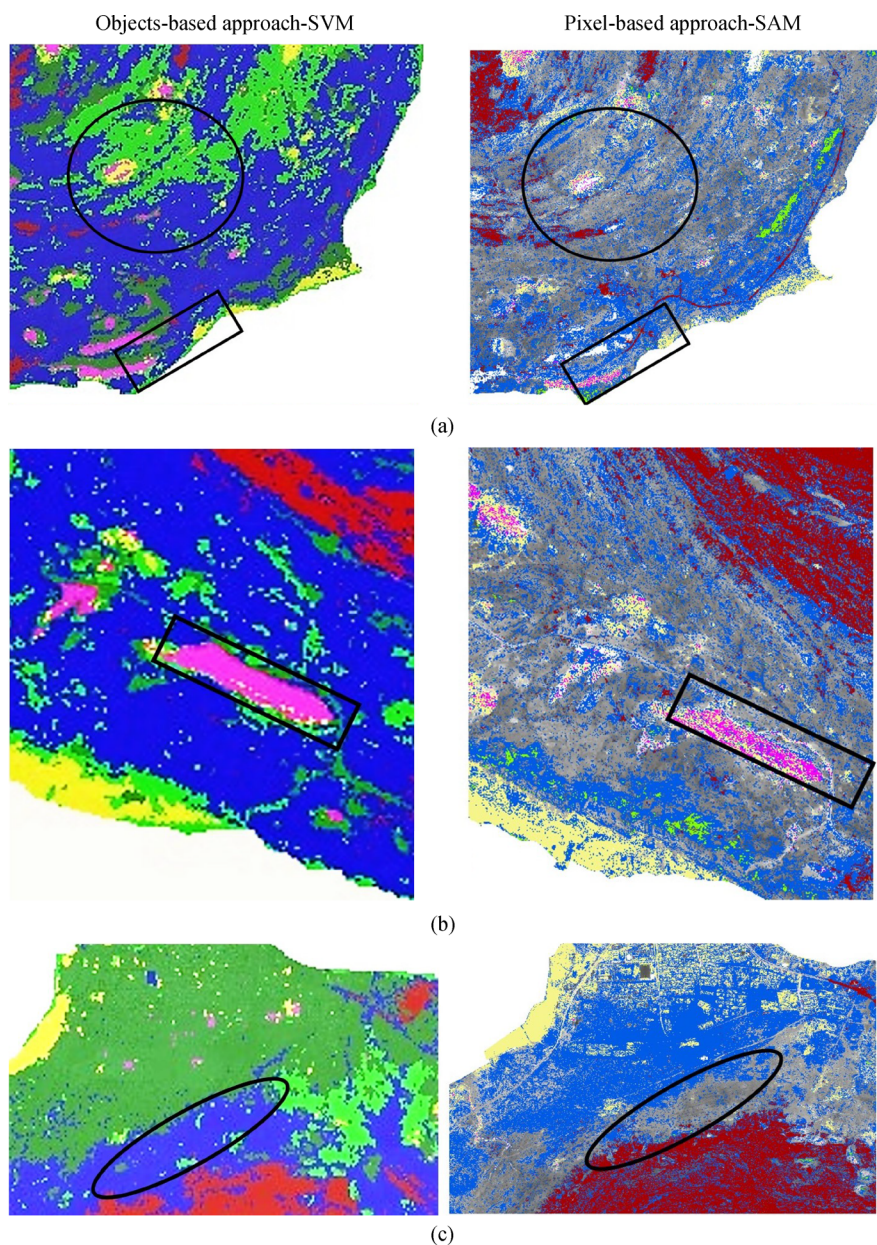


Fig. 11 Comparison of results achieved by object-based and pixel-based approaches: a) improvement in lithological mapping outcrops, b) omission of ambiguous mixture, and c) filtering salt and-pepper pixel in a mixture of red soil, gypsum, and anhydrite.

all the pixels of a given object are averaged. This leads in decreasing the mapping confusion by decreasing the variations within an object. An essential disadvantage of a pixel-based mapping method is that it does not use the data of neighboring pixels to support more correctly recognition of a target class for a pixel. Consequently, if pixels of a class of lithology exhibit local spectral heterogeneity, they may be labeled as different classes. Therefore, the pixel-based methods could obtain a high rate of misclassification such that specific regions of a class of rock might wrongly be classified as another rock unit. Furthermore, if per-pixel methods are applied, usage of imagery with high spatial resolution, such as WV-3, which is needed to separate the small areas of specific rock units, may lead to increased errors in classifications.

This study aimed to classify the lithological groups of a geologically complex terrain by focusing on the high spatial resolution of WV-3 VNIR data. This advantage of WV-3 led to successful enhancement of lithological boundaries in the study area, including places where lithology is not homogeneous, and the outcrops are small. Another investigation has also suggested the advantageous usage of the spatial resolution of WV-3 in mapping the geological targets (Sun et al., 2017). Bedini (2019) showed that integration of WV-3 and ASTER TIR data could successfully recognize the lithological units by using spectral properties and indices calculated from WV-3 imagery.

Although in this study, we proved the advantage of the OBIA method in comparison to the PBIA approach for an improved lithological mapping using only the VNIR bands of WV-3, further works to consider the SWIR bands of this satellite is recommended.

Although it is suggested that considering absorption features in the segmentation process gives satisfactory results (Grebby et al., 2016), their application could be more various than region growing. This research emphasizes the efficiency of object-based image analysis in reducing the spectral variability within an object (here, lithology) and the conjunction of supplementary information extracted from structural and contextual image/object properties to improve the enhancement of rock units.

5 Conclusions

This study was a comparative approach to show the capabilities of pixel-based and object-based methods and their representative algorithms, SAM and SVM, in discriminating the lithological classes using VNIR data of WorldView-3 of Hormuz Island, southern Iran. Results obtained by these two approaches revealed that the OBIA method was superior compared to the PBIA method. The OBIA could lead to an improved discrimination of lithological groups, clear detection of geological units with complex lithology such as Quaternary deposits, and

successful decrease or remove of salt-and-pepper pixels, which were common in spectral-based output map.

Comparing the degree of efficacies of applied methods illustrated that the object-based approach basically conforms to a type of expert interpretation aiming to find out the internal relationships among neighboring pixels. This advantage leads to a relatively perfect classification of features, while that of the pixel-based approach is segregated. Furthermore, the WV-3 data, because of its high spatial resolution, is notably suitable for the OBIA approach aiming the discrimination and classification of lithological units in a geologically complex district. Moreover, realizing the same ideal texture groups by SVM method is a basis for lithological mapping and classifying. It was shown that the OBIA approach produces a more improved and contiguous lithological map than the PBIA method. Overview of the criteria mentioned above showed that pixel size of 1.24 m for VNIR bands of WV-3 is particularly advantageous for lithological mapping by using the OBIA method rather than the PBIA method.

References

- Aqanabati S A (2006). Geology and mineral potential of Hormozgan Province. *Journal of Development of Geology Training*, 12: 4–11
- Ayoobi I, Tangestani M H (2018). Evaluation of subpixel unmixing algorithms in mapping the porphyry copper alterations using EO-1 Hyperion data, a case study from SE Iran. *Remote Sensing Applications: Society and Environment*, 10: 120–127
- Aufaristama M, Hölbling D, Höskuldsson A, Jónsdóttir I (2017). Comparison of SAM and OBIA as tools for lava morphology classification—a case study in Krafla, NE Iceland. In: EGU General Assembly, 19
- Blaschke T (2010). Object based image analysis for remote sensing. *ISPRS J Photogramm Remote Sens*, 65(1): 2–16
- Blaschke T, Strobl J (2001). What's wrong with pixels? Some recent developments interfacing remote sensing and GIS. *GIS – Zeitschrift für Geoinformations systeme* 14(6), 12–17
- Blaschke T, Burnett C, Pekkarinen A (2004). New contextual approaches using image segmentation for object-based classification. In: De Meer F, de Jong S, eds. *Remote Sensing Image Analysis: Including the spatial domain*. Dordrecht: Kluwer Academic Publishers, 211–236
- Bedini B (2019). Application of WorldView-3 imagery and ASTER TIR data to map alteration minerals associated with the Rodalquilar gold deposits, southeast Spain. *Adv Space Res*, 63(10): 3346–3357
- Boardman J W, Kruse F A (1994). Automated spectral analysis: a geologic example using AVIRIS data, north Grapevine Mountains, Nevada. In: Tenth Thematic Conference on Geologic Remote Sensing, Environmental Research Institute of Michigan, Ann Arbor, MI
- Bahrambeygi B, Moeinzadeh H (2017). Comparison of support vector machine and neural network classification method in hyperspectral mapping of ophiolite mélanges—a case study of east of Iran. *Egypt J*

- Remote Sens Space Sci, 20(1): 1–10
- Burges C J C, (1998). A tutorial on support vector machines for pattern recognition. *Data Mining and Knowledge Discovery* 2: 121–167
- Bolouki S M, Ramazi H R, Maghsoudi A, Beiranvand Pour A, Sohrabi G (2019). A remote sensing-based application of bayesian networks for epithermal gold potential mapping in Ahar-Arasbaran Area, NW Iran. *Remote Sens*, 12(1): 105
- Benz U C, Hofmann P, Willhauck G, Lingenfelder I, Heynen M (2004). Multiresolution, object-oriented fuzzy analysis of remote sensing data for GIS-ready information. *ISPRS J Photogramm Remote Sens*, 58(3–4): 239–258
- Congalton R G, Green K (2009). *Assessing the Accuracy of Remotely Sensed Data: Principles and Practices*. Boca Raton: CRC Press
- Castillejo-González I L, López-Granados F, García-Ferrer A, Peña-Barragán J M, Jurado-Expósito M, de la Orden M S, González-Audicana M (2009). Object- and pixel-based analysis for mapping crops and their agro-environmental associated measures using QuickBird imagery. *Comput Electron Agric*, 68(2): 207–215
- Clark R N, Roush T L (1984). Reflectance spectroscopy: quantitative analysis techniques for remote sensing applications. *J Geophys Res Solid Earth*, 89(B7): 6329–6340
- Cai J, Luo J, Wang S, Yang S (2018). Feature selection in machine learning: a new perspective. *Neurocomputing*, 300: 70–79
- Dorren L K, Maier B, Seijmonsbergen A C (2003). Improved Landsat-based forest mapping in steep mountainous terrain using object-based classification. *Forest Ecology and Management*, 183 (1–3): 31–46.
- Darwish A, Leukert K, Reinhardt W (2003). Image segmentation for the purpose of object-based classification. In: *Geoscience and Remote Sensing Symposium, IGARSS'03. 2003 IEEE International*, (3): 2039–2041
- Ducart D F, Silva A M, Toledo C L B, Assis L M (2016). Mapping iron oxides with Landsat-8/OLI and EO-1/ Hyperion imagery from the Serra Norte iron deposits in the Carajás Mineral Province, Brazil. *Braz J Geol*, 46(3): 331–349
- Elnagheeb A H, Bromley D W (1994). Extensification of agriculture and deforestation: empirical evidence from Sudan. *Agricultural Economics* 10(2): 193–200
- Fakhari M (1994). *Geological Quadrangle Map of Bandar-Abbas, 1:250000. Sheet No. 1–13*, National Iranian Oil Company
- Elyasi J, Aminsobhani E, Behzad A, Moenvaziri H, Meysami A (1975). *Geology of Hormuz Island*. Geological Survey of Iran Publication, Tehran, 1: 13
- Grebby S, Field E, Tansey K (2016). Evaluating the Use of an Object-Based Approach to Lithological Mapping in Vegetated Terrain. *Remote Sens*, 8(10): 843
- Gasmi A, Gomez C, Zouari H, Masse A, Ducrot D (2016). PCA and SVM as geo-computational methods for geological mapping in the southern of Tunisia, using ASTER remote sensing data set. *Arab J Geosci*, 9(20): 753
- Huang C K, Kerr P F (1960). Infrared study of the carbonate minerals, *Am Mineral*, 45: 311–324
- Hunt G R (1980). Electromagnetic radiation: the communication link in remote sensing. In: Siegal BS, Gillepie AR, eds, *Remote Sensing in Geology*, Wiley: New York, 5–45
- Hewson R D, Robson D, Carlton A, Gilmore P (2017). Geological application of ASTER remote sensing within sparsely outcropping terrain, Central New South Wales, Australia. *Cogent Geosci*, 3(1): 1319259
- Hay G J, Castilla G (2008). Geographic object-based image analysis (GEOBIA): a new name for a new discipline. In: Blaschke T, Lang S, Hay G, eds, *Object Based Image Analysis*. Heidelberg: Springer, 93–112
- Hay G J, Niemann K O (1994). Visualizing 3-D texture: a three dimensional structural approach to model forest texture. *Can J Rem Sens*, 20(2): 90–101
- Ibrahim E, Barnabé P, Ramanaidou E, Pirard E (2018). Mapping mineral chemistry of a lateritic outcrop in New Caledonia through generalized regression using Sentinel-2 and field reflectance spectra. *Int J Appl Earth Obs Geoinformation*, 73: 653–665
- Jensen J R (2005). *Introductory Digital Image Processing*. Upper Saddle River: Person Prentice Hall
- Karatzoglou A, Smola A, Hornik K, Zeileis A (2004). Kernlab – an R package for kernel methods in R. *J Stat Softw*, 11(9): 1–20
- Kuester M (2016). Radiometric use of WV-3 imagery. Technical Note. DigitalGlobe
- Kavzoglu T, Colkesen I (2009). A kernel functions analysis for support vector machines for land cover classification. *Int J Appl Earth Obs Geoinf*, 11(5): 352–359
- Kruse F A, Lefkoff A B, Boardman J B, Heidebrecht K B, Shapiro A T, Barloon P J, Goetz A F H (1993). The Spectral Image Processing System (SIPS)—interactive visualization and analysis of imaging spectrometer data. *Remote Sens Environ*, 44(2-3): 145–163
- Lang S, Schöpfer E, Langanke T (2008). Combined object-based classification and manual interpretation — synergies for a quantitative assessment of parcels and biotopes. *Geocarto Int*, 23(4): 1–16
- Liu L, Feng J, Rivard B, Xu X, Zhou J, Han L, Yang J, Ren G (2018). Guangli Ren Mapping alteration using imagery from the Tiangong-1 hyperspectral spaceborne system: example for the Jintanzi gold province, China. *Int J Appl Earth Obs Geoinf*, 64: 275–286
- Marceau D (1999). The scale issue in the social and natural sciences. *Can J Rem Sens*, 25(4): 347–356
- Mahyari M G (2016). Comparison of ASTER reflective and thermal infrared data for discriminating lithological units and identifying potash-bearing areas in Hormoz salt plug. Dissertation for Master's Degree. Shiraz: Shiraz University
- Matton G S, Canto F, Waldner S, Valero D, Morin J, Inglada M, Arias S, Bontemps B, Koetz P, Defourny P (2015). DefournyAn automated method for annual cropland mapping along the season for various globally-distributed agrosystems using high spatial and temporal resolution time series. *Remote Sens*, 7(10): 13208–13232
- Melgani F, Bruzzone L (2004). Classification of hyperspectral remote sensing images with support vector machines. *IEEE Trans Geosci Remote Sens*, 42(8): 1778–1790
- Marceau D J, Howarth P J, Dubois J M M, Gratton D J (1990). Evaluation of the grey level co-occurrence matrix method for land-cover classification using SPOT imagery. *IEEE Trans Geosci Remote Sens*, 28(4): 513–519
- Mars J C (2018). Mineral and lithologic mapping capability of WorldView 3 data at Mountain Pass, California, using true- and false-color composite images, band ratios, and logical operator algorithms. *Econ Geol*, 113(7): 1587–1601
- Mason D C, Corr D G, Cross A, Hogg D C, Lawrence D H, Petrou M,

- Taylor A M (1988). The use of digital map data in the segmentation and classification of remotely-sensed images. *Int J Remote Sens*, 2: 195–215
- Mather P M, Tso B, Koch M (1998). An evaluation of Landsat TM spectral data and SAR-derived textural information for lithological discrimination in the Red Sea Hills, Sudan. *Int J Remote Sens*, 19(4): 587–604
- Markoski P R, Rolim S B A (2014). Evaluation of ASTER images for characterization and mapping of volcanic rocks (Basalts). *International Journal of Advanced Remote Sensing and GIS*, 3(1): 486–498
- Mengisteab B S, Blesius L, Hennessy L (2014). Application of object based image analysis (OBIA) in detection and quantifying forest loss caused by artisanal gold mining activities in Upper Mazaruni River Basin, Guyana. In: AGU Fall Meeting, 2014
- Noori L, Pour B A, Askari G, Taghipour N, Pradhan B, Lee C W, Honarmand M (2019). Comparison of different algorithms to map hydrothermal alteration zones using ASTER remote sensing data for polymetallic vein-type ore exploration: toroud-chahshirin magmatic belt (TCMB). North Iran. *Remote Sensing*, 11(5): 495
- Naghadehi K M, Hezarkhani A, Asadzadeh S (2014). Mapping the alteration footprint and structural control of Taknar IOCG deposit in east of Iran, using ASTER satellite data. *Int J Appl Earth Obs Geoinf*, 33: 57–66
- Oommen T, Misra D, Twarakavi N K C, Prakash A, Sahoo B, Bandopadhyay S (2008). An objective analysis of support vector machine based classification for remote sensing. *Math Geosci*, 40(4): 409–424
- Petitjean F, Kurtz C, Passat N, Gançarski P (2012). Spatio-temporal reasoning for the classification of satellite image time series. *Pattern Recognit Lett*, 33(13): 1805–1815
- Petropoulos G P, Vadrevu K, Kalaitzidis Ch (2012). Spectral Angle Mapper and Object-based classification combined with hyperspectral remote sensing imagery for obtaining land use/cover mapping in a Mediterranean region. *Geocarto Int*, 28(2)
- Qiu F, Abdelsalam M, Thakkar P (2006). Spectral analysis of ASTER data covering part of the Neoproterozoic Allaqi-Heiani suture, Southern Egypt. *J Afr Earth Sci*, 44(2): 169–180
- Richards J A (1993). *Remote Sensing Digital Image Analysis: An Introduction*. 2nd ed. Berlin Heidelberg: Springer-Verlag
- Rajendran S, Nasir S (2019). ASTER capability in mapping of mineral resources of arid region: a review on mapping of mineral resources of the Sultanate of Oman. *Ore Geol Rev*, 108: 33–53
- Research Systems, Inc. (2002). *ENVI Tutorials*. Boulder: Research Systems, Inc
- Rajendran S, Nasir S, Kusky T M, Ghulam A, Gabr S, El Ghali M (2013). Detection of hydrothermal mineralized zones associated with listwaenites in Central Oman using ASTER data. *Ore Geol Rev*, 53: 470–488
- Stocklin J (1972). *Lexique Stratigraphique International*. Geological Survey of Iran Publication, Tehran, 36: 15
- Faramarzi N S, Amini S, Schmitt A K, Hassanzadeh J, Borg G, McKeegan K, Razavi S M H, Mortazavi S M (2015). Geochronology and geochemistry of rhyolites from Hormuz Island, southern Iran: a new record of Cadomian arc magmatism in the Hormuz Formation. *Lithos*, 236–237: 203–211
- Stocklin J (1974). Possible ancient continental margins in Iran. In: *The Geology of Continental Margins*. Berlin: Springer, 873–887
- Salisbury J W, Hunt G R (1974). Remote sensing of rock type in the visible and near infrared. In: *Proceedings of 9th International Symposium on Remote Sensing Environment*, Ann Arbor, vol III, 1953–1958
- Sun Y, Tian S, Di B (2017). Extracting mineral alteration information using Worldview-3 data. *Geoscience Frontiers*, 8(5): 1051–1062
- Segal D B (1983). Use of Landsat multispectral scanner data for the definition of limonitic exposures in heavily vegetated areas. *Econ Geol*, 78(4): 711–722
- Thapa R B, Murayama Y (2009). Urban mapping, accuracy, and image classification: a comparison of multiple approaches in Tsukuba City, Japan. *Applied Geography* 29:135–144
- Testa F J, Villanueva C, Cooke D, Zhang L (2018). Lithological and Hydrothermal Alteration Mapping of Epithermal, Porphyry and Tourmaline Breccia Districts in the Argentine Andes Using ASTER Imagery. *Remote Sens*, 10(2): 203
- Tormos T, Kosuth P, Durrieu S, Dupuy S, Villeneuve B, Wasson J (2012). Object-based image analysis for operational fine-scale regional mapping of land cover within river corridors from multi-spectral imagery and thematic data. *Int J Remote Sens*, 33(14): 4603–4633
- Trimble (2015). *eCognition Developer 9.1 User Guide*. Munich: Trimble Documentation
- Van der Werff H, Van Ruitenbeek F, Zegers T, Van der Meer F (2007). Geologic mapping on Mars by segmentation of OMEGA data. In: *Proceedings 5th EARSeL Workshop on Imaging Spectroscopy*
- Wang L, Sousa W, Gong P (2004). Integration of object-based and pixel-based classification for mangrove mapping with IKONOS imagery. *Int J Remote Sens*, 25(24): 5655–5668
- Ye B, Tian S, Ge J, Sun Y (2017). Assessment of WorldView-3 Data for Lithological Mapping. *Remote Sens*, 9(11): 1132
- Yazdi A, Arian M A, Tabari M M R (2014). Geological and geotourism study of Iran Geology Natural Museum, Hormoz Island. *Open J Ecol*, 4(11): 703–714
- Yeomans C, Middleton M, Shail R K, Grebby S, Lusty P A J (2019). Integrated Object-Based Image Analysis for semi-automated geological lineament detection in southwest England. *Comput Geosci*, 123: 137–148